



**HAL**  
open science

## Improving Spatial and Elemental Associations in Analytical Field Ion Microscopy

Felipe F Morgado, Leigh Stephenson, Loïc Rousseau, François Vurpillot, Simon Evertz, Jochen M Schneider, Baptiste Gault

► **To cite this version:**

Felipe F Morgado, Leigh Stephenson, Loïc Rousseau, François Vurpillot, Simon Evertz, et al.. Improving Spatial and Elemental Associations in Analytical Field Ion Microscopy. *Microscopy and Microanalysis*, 2023, 29, pp.1077-1086. 10.1093/micmic/ozad039 . hal-04056079

**HAL Id: hal-04056079**

**<https://normandie-univ.hal.science/hal-04056079>**

Submitted on 3 May 2023

**HAL** is a multi-disciplinary open access archive for the deposit and dissemination of scientific research documents, whether they are published or not. The documents may come from teaching and research institutions in France or abroad, or from public or private research centers.

L'archive ouverte pluridisciplinaire **HAL**, est destinée au dépôt et à la diffusion de documents scientifiques de niveau recherche, publiés ou non, émanant des établissements d'enseignement et de recherche français ou étrangers, des laboratoires publics ou privés.

# Improving spatial and elemental associations in analytical field ion microscopy

Felipe F. Morgado,<sup>1</sup> Leigh Stephenson,<sup>1</sup> Loic Rousseau,<sup>2</sup> François Vurpillot,<sup>2</sup> Simon Evertz,<sup>1,3</sup> Jochen M Schneider,<sup>3</sup> and Baptiste Gault<sup>1,4</sup>

<sup>1</sup>Max-Planck-Institut für Eisenforschung, Max-Planck-Str. 1, 40237, Düsseldorf, Germany

<sup>2</sup>Normandie Université, UNIROUEN, INSA Rouen, CNRS, Groupe de Physique des Matériaux, Rouen 76000, France

<sup>3</sup>Materials Chemistry, RWTH Aachen University, Kopernikusstr. 10, 52074 Aachen, Germany

<sup>4</sup>Department of Materials, Royal School of Mines, Imperial College London, London, SW7 2AZ, UK

Corresponding Author: Felipe F. Morgado | Baptiste Gault <f.ferraz@mpie.de | b.gault@mpie.de>

## Abstract

Chemically resolved atomic-resolution imaging can give fundamental information about material properties. However, even today, a technique capable of such achievement is still only an ambition. Here, we take further steps in developing the analytical field ion microscopy (aFIM), which combines the atomic spatial resolution of field ion microscopy (FIM) with the time-of-flight spectrometry of atom probe tomography (APT). To improve the performance of aFIM that are limited in part by a high level of background, we implement bespoke flight-path time-of-flight corrections normalised by the ion flight distances traversed in electrostatic simulations modeled explicitly for an atom probe chamber. We demonstrate effective filtering in the field evaporation events upon spatially- and temporally-correlated multiples, increasing the mass spectrum's signal-to-background. In an analysis of pure tungsten, mass peaks pertaining to individual W isotopes can be distinguished and identified, with the signal-to-background improving by three orders of magnitude over the raw data. We also use these algorithms for the analysis of a CoTaB amorphous

film to demonstrate application of aFIM beyond pure metals and binary alloys. These approaches facilitate elemental identification of the FIM-imaged surface atoms, making analytical FIM more precise and reliable.

**Key Words:** atom probe tomography, analytical field ion microscopy, atomic resolution, time-of-flight spectrometry, Correlation filtering (Received XX Y 20ZZ; revised XX Y 20ZZ; accepted XX Y 20ZZ)

## Introduction

Atomic resolution imaging can provide unique information regarding a material's structure to link it to its intrinsic properties and help gain insights necessary to guide the design of future materials (Robertson & Warner (2013); Zhang et al. (2017); Wei et al. (2021)). By coupling the atomic spatial resolution with chemical information, it should be, in principle, possible to study the structure and chemistry of structural defects that remain a grand challenge for the microscopy community.

Field-ion microscopy (FIM) was the first technique to image individual atoms on a metal surface in the 1950s (Müller (1951, 1956)). Its working principle is based on the field ionisation of an imaging gas in the vicinity of the surface of a sharp, needle-shaped specimen usually at cryogenic temperatures to improve spatial resolution by the electrostatic field arising from biasing the specimen to a high voltage (Block (1994)). This field of the order of a few tens  $V/nm$  causes field adsorption of the imaging gas onto the field emitter surface, which greatly influences field ionisation (Schmidt (1994); Tsong (1990); Sweeney & Tsong (1981)). The electrostatic field strength that gives the clearest image and possibly atomic resolution is termed the best imaging field (BIF) (Müller (1961)). Furthermore, the adsorbed imaging gas and the surface atoms can also be field desorbed or field evaporated in the form of ions. This field evaporation can then be time-controlled using pulsed voltage or pulsed laser from which a 3D-FIM reconstruction can be made (Müller et al. (1969); Müller et al. (1968); Cerezo et al. (2007); Vurpillot et al. (2017)).

Müller et al. (1968) later introduced the concept of atom-probe field ion microscopy (AP-FIM), a field-ion microscope augmented by a time-of-flight spectrometer to analyse, i.e., reveal the elemental nature of target individual or small groups of atoms from the surface of the specimen after removal of the imaging gas. AP exploits the field evaporation of ions from a sharp needle specimen's surface via voltage (Müller et al. (1968)) or laser pulsing (Kellogg & Tsong (1980); Jentsch et al. (1981), Kellogg et al. (1979)). A time-of-flight spectrometer enables the ion's mass-to-charge ratio to be determined.

Atom probe tomography (APT), which has become more widely used in the past two decades, later evolved from APFIM. In APT, a position-sensitive detector records the spatial coordinates of the collected ion along with the time-of-flight. As a result, a chemically resolved three-dimensional reconstruction with a sub-nanometre spatial resolution is obtained (Gault et al. (2012a, 2021a), Larson et al. (2013a)). APT is widely used to study a material's microstructure to establish relationships between its composition, processing history and set of physical properties (Miller (2005); Seidman (2007); Kim et al. (2021); Kelly & Larson (2012)).

Compositional mapping with true atomic resolution has been targeted since the early developments of atom-probe FIM (Müller et al. (1968)), yet trajectory aberrations present in the field evaporation process impede progress towards this goal (Krishnaswamy et al. (1975); Miller, M.K. (1987); Gault et al. (2021b)). Promising results have been obtained with a few different approaches, such as X-ray energy-dispersive spectroscopy combined with scanning transmission electron microscopy. However, transmission microscopy techniques are usually limited to atomic-column resolution (Itakura et al. (2013); Allen et al. (2012); Goris et al. (2013)) or require computationally costly models to retrieve the information (Zhou et al. (2019)). These also suffer from limitations in the range of sample geometry and elements that can be imaged by transmission electron microscopy.

Building upon the APFIM concept, analytical FIM (aFIM) was recently proposed as an

alternative technique to APT (Katnagallu et al. (2019, 2021)). An aFIM experiment is performed in a modern atom probe microscope, yet under a higher pressure of a gas typically used for imaging in FIM. This is not to be confused with electronic FIM (eFIM), which uses the same instrumental platform but only provides emulated images based on impacts on the particle detector operated in an imaging mode of the atom probe microscope, and eFIM has no analytical capabilities. AFIM, in principle, allows for combining the atomic resolution of FIM, through the field ionisation of the imaging gas atoms, with the time-of-flight mass spectrometry analysis performed across the wide-field-of-view of modern atom probe microscopes and not just through a probe-hole like for APFIM. AFIM experimentation has a considerable, yet undeveloped, potential for the characterisation of certain materials, particularly the interactions of solute elements with structural defects, including vacancies (Morgado et al. (2021)) and dislocations (Katnagallu et al. (2019)) for which APT's spatial resolution is insufficient.

As compared to APT experiments, the unusually higher working pressure ( $10^{-8} - 10^{-6}$  mbar) due to the imaging gas causes a very high level of background in the mass spectrum. Moreover, the commonly used algorithms integrated into commercial software to process the raw data often fail to identify peaks and hence perform the necessary voltage correction (Sebastian et al. (2001)) and the so-called bowl correction (Larson et al. (2013)) to account for changes in the flight length as a function of the ion's emitting angle. Furthermore, with a high background, it might be challenging to identify the peaks in the mass spectrum to assign an elemental identity to the field evaporated ions, as the peaks may not be high enough above the background and therefore be indistinguishable in the spectrum. As a result, processing aFIM data can be extremely challenging, and these difficulties hinder the precise identification of the surface atoms' elemental nature.

Here, we aim to develop the processing of aFIM data further. We focus on experimental data obtained from pure tungsten and a CoTaB metallic glass film. First, we propose a new algorithm for

the time-of-flight bowl corrections by using an initial input obtained from calculating the distance travelled by the emitted ions using electrostatic simulations. Second, we introduce an approach that exploits spatial and temporal correlations for data filtering, leading to a substantial decrease in the background found on the mass spectrum. These improvements make it easier to chemically identify the field evaporated ions among the field ionisation events and, hence, help make aFIM analyses increasingly more routine.

## **Materials and Methods**

### ***Materials***

Needle-shaped specimens for analytical field ion microscopy were prepared from pure tungsten to test the technique's limits by electrochemical polishing at 5-8 VAC in a 5% molar NaOH solution using the conventional approach outlined in (Müller & Tsong (1969); Miller & Forbes (2014)).

Samples from a ternary amorphous alloy  $Co_{68}Ta_7B_{25}$  film were also analysed. Details of the sample's fabrication can be found in Refs. (Schnabel et al. (2016); Kontis et al. (2018); Evertz et al. (2020)). In short, a magnetron sputtering ultrahigh vacuum chamber was used to sputter targets of a  $Co_{88}Ta_{12}$  alloy and an elemental target of B with different power densities directly on a Si (001) wafer with a diameter of 50.8 mm. This sample was selected because B, Co, and Ta only have 1–2 isotopes and cover a wide range of mass-to-charge ratios, from 5 Da for  $10B^{2+}$  and up to 181 Da for  $181Ta^{1+}$ , which is unlikely to be detected in the range of fields necessary to field evaporate the majority species  $Co^{79}$  (Kingham (1982)).

### ***Analytical Field Ion Microscopy***

The aFIM arises from the combination of the APT and eFIM or digital FIM. We use the Cameca local electrode atom probe (LEAP) 5000 XS equipped with the eFIM module. Conversely to eFIM, in aFIM each detector hit is associated with the corresponding time-of-flight measurement using the

APT acquisition mode. By manually introducing the imaging gas (e.g., He, Ar, or Ne) via a leak valve, the imaging pressure is adjusted to around  $10^{-7}$  mbar. The pressure typically decreases over the course of the experiment due to cryo-trapping and a lack of any feedback system to admit more gas in response.

Given the high applied field, the imaging gas can be adsorbed on the specimen's surface. And as the field increases, it eventually desorbs, usually linked to the field evaporation of the surface atoms. In short, the main parameters for such experiments are the gas composition, the pressure, the amplitude of the pulsed voltage, and the base specimen temperature. Having fine control of these parameters is important to optimise the contrast in the field ion micrograph, enable imaging of even the dimmest atom, and control the field evaporation of the surface atoms. One way to manage this dynamic is by using a voltage pulse or laser pulse superimposed to the best imaging voltage (Katnagallu et al. (2021)).

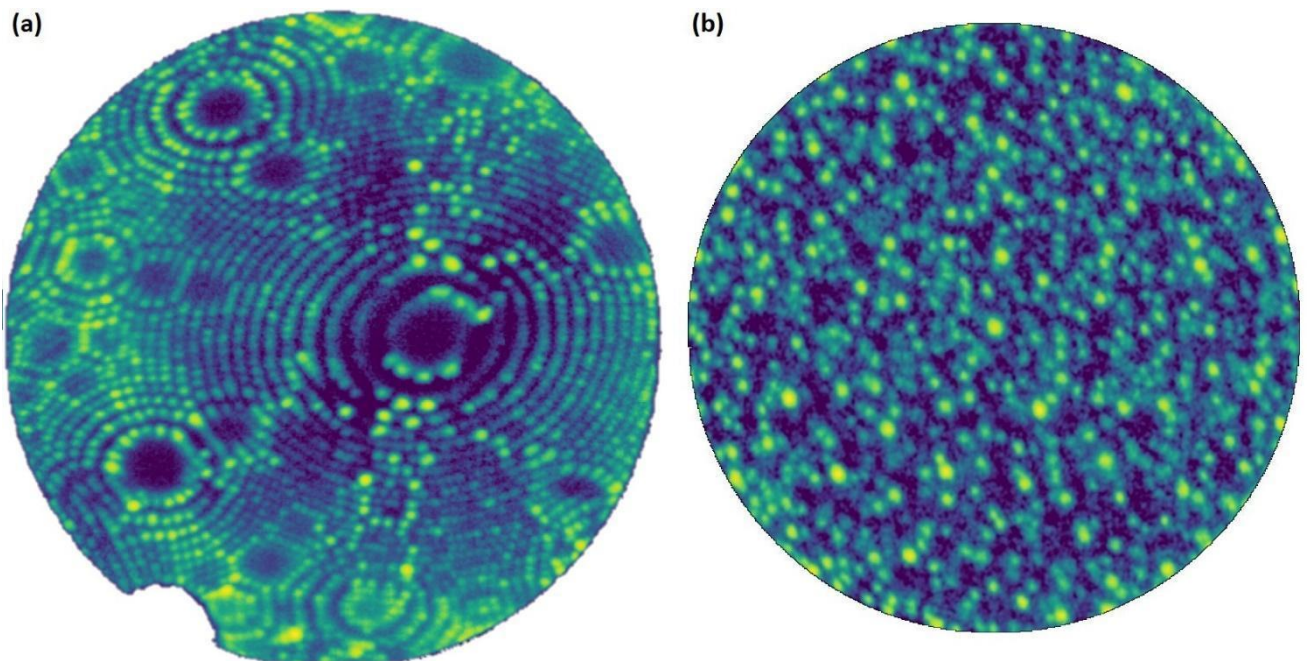


**Fig. 1.** AFIM image formed from the field ionised events on the APT detector with Ne imaging gas of the (a) bcc tungsten tip and the (b) metallic glass  $Co_{68}Ta_7B_{25}$  film.

Lastly, the data is extracted as an extended-POS ".EPOS" file using the commercial software AP

Suite 6.1. This file contains the reconstructed position (x,y,z), the mass-to-charge ratio (Da), raw time of flight, standing voltage, pulsed voltage, detector coordinates of the ions (x,y), number of pulses since last detected ion and multiplicity ions. More details about the system can be found in Katnagallu et al. (2021). The aFIM experiments were conducted using the pulsing voltage mode with a pulse fraction of 20% and a 99.999% pure Ne as imaging gas. The pressure in the CoTaB experiment changed from  $10^{-7}$  to  $5 \times 10^{-8}$  mbar in the ultrahigh vacuum chamber, and the pulse repetition rate was set to 65 kHz to guarantee that all atoms were imaged by field ionised gas at the DC voltage before getting field evaporated by the voltage pulse. The data analysis of the EPOS files (more specifically, mass-to-charge ratio, raw time of flight, standing voltage, detector coordinates, number of pulses since last ion and multiplicity) was performed using algorithms developed in-house with MATLAB R2019a.

Figure 1 shows the FIM image recreated from the field ionised events of aFIM experiments. Figure 1(a) is a FIM micrograph revealing a tungsten tip's 011-orientated bcc lattice structure. In contrast, Figure 1(b) is a FIM micrograph of the amorphous alloy  $Co_{68}Ta_7B_{25}$  film, and no crystalline features can be seen.

## Results

Ions of the same mass-to-charge projected away from the specimen at different emitting angles by the divergent field generated by the specimen fly along trajectories of different curvilinear length. The ions are hence detected with different TOF measurements on the distant planar detector. A "bowl" correction on measured time-of-flight data accounts for longer flight paths for ions that impact away from the detector centre (Larson et al. (2013)). Meanwhile, the aFIM experiments can be described as APT experiments under higher pressures, given the imaging gas in the vacuum chamber. As such, similar corrections must be applied to the data.

### *Time-of-flight bowl correction*

For atom probe instruments with a small field-of-view (FOV), the TOF errors could be satisfactorily corrected using the Pythagoras theorem to relate a detector impact position to a flight path length (Pareige et al. (2016)). However, new algorithms needed to be implemented with the increase in the FOV from a reduction in the distance between the specimen and the detector (Deconihout et al. (2007)), particularly on the local electrode atom probe (Kelly et al. (2004)). The commercial software package IVAS uses two iterative procedures for the voltage (Sebastian et al. (2001)) and bowl corrections, aiming to decrease the width of typically the highest peaks in the TOF spectrum Larson et al. (2013). These approaches require the selection of this peak, which can be very difficult and usually fails for aFIM experiments due to the low signal-to-background. Furthermore, improvements from the voltage correction are typically modest as, for most aFIM experiments, the span of high voltage is relatively small (e.g., 5% of the final standing voltage).

The approach for the bowl TOF correction we introduce herein is based on the electrostatic simulations from Loi et al. (2013). The flight distance ( $L_{\text{flight}}$ ) travelled by the ions emitted from the specimen's surface at increasing angles was calculated by integrating the actual path they followed during the flight toward the detector. This flight distance is then plotted against the detector impact radial coordinates ( $r$ ) on the virtual detector for each combination of the **shape of the tip, such as the radius of curvature at the specimen apex** (20-160 nm) and **the angle of the specimen's cone or shank angle** (2-18°), represented as various colours and symbols in Figure 2, respectively. As all the data points fall on a similar trend, these are not detailed. A polynomial fit via a least-square protocol was calculated for each set of data, with  $R^2 \approx 1$  for each data series. A final polynomial is calculated based on the average of the fitting parameters from all the fits. Figure 2 (inset) shows the ratios of the actual flight distance to the predicted from the polynomial fit for each data set, this average polynomial, and from the Pythagoras theorem. **Alternatively, the algorithm could be also derived experimentally via APT experiments, similar to what is done by the manufacturer for the calibration**

of the instrument.

As these simulations had been performed for an earlier configuration of the LEAP (3000/4000 generation), we used some sets of simulations from Lorentz-2E V10.2 reported in Ref. Rousseau et al. (2020) for a geometry of a LEAP 5000 XS. Based on this polynomial deduced from the fitting procedure,  $L_{flight}$  (m) can be obtained from this formula (Equation 1):

$$L_{flight} = 847.25r^5 - 198.35 r^4 + 0.45 r^3 + 5.56 r^2 + 9.84 \times 10^{-6}r + 0.10 \quad (1)$$

where each coefficient is determined from the fitting procedure for this specific instrument.

Polynomials with higher degrees were also tried but did not lead to an improvement in the  $R^2$  value.

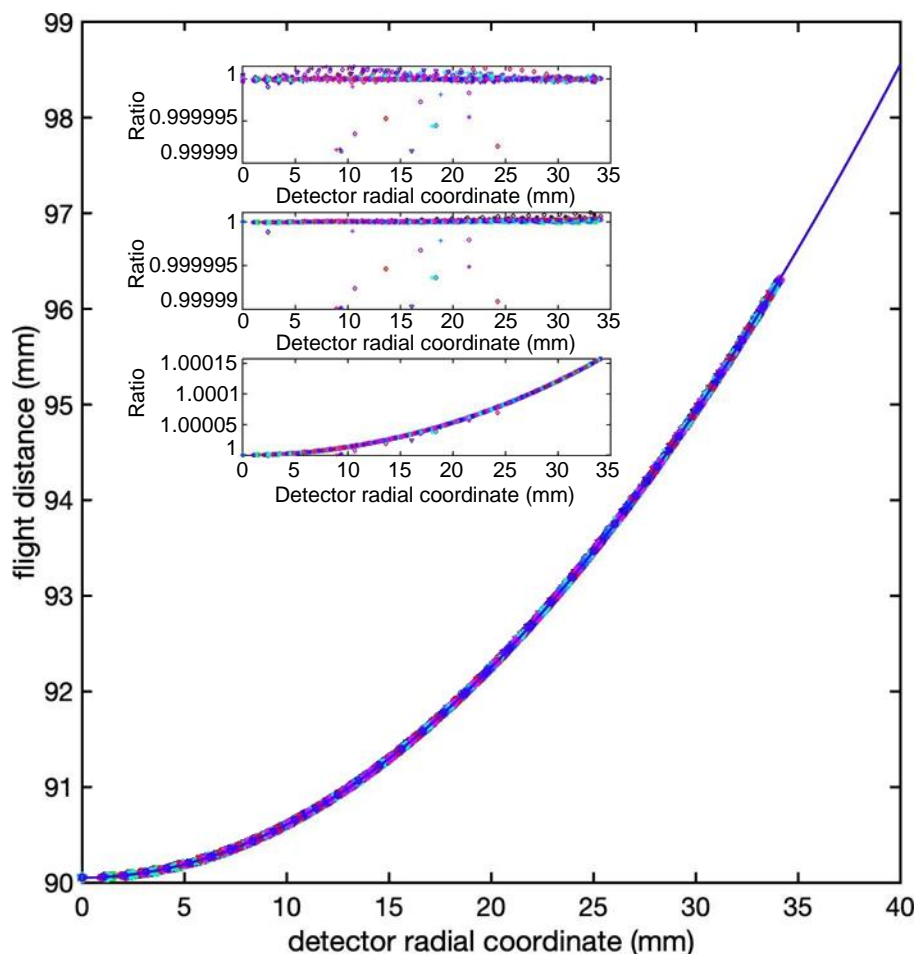
The conversion from the corrected TOF to mass-to-charge ratio is given by:

$$\frac{m}{n} = \frac{2eV(t_{flight}-t_0)^2}{L^2_{flight}} \quad (2)$$

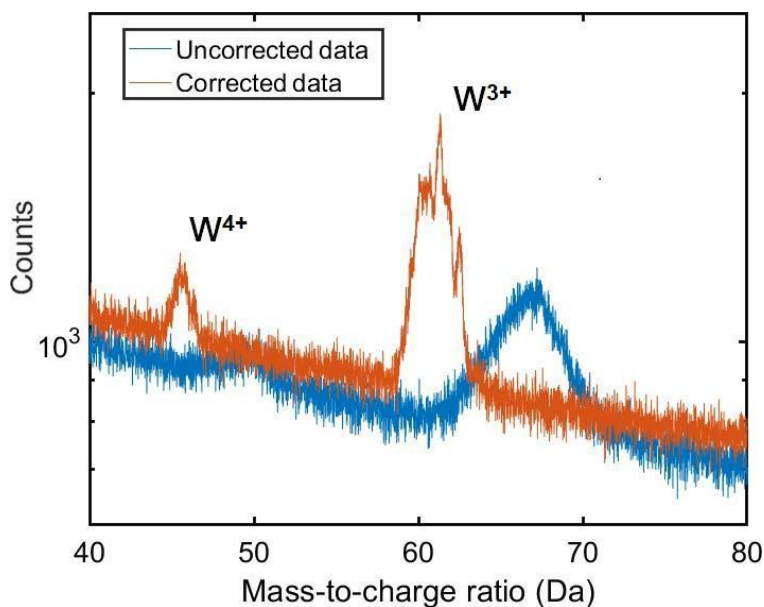
where  $e$  is the electron charge,  $n$  is the charge state,  $V$  is the applied voltage,  $t_{flight}$  and  $L_{flight}$  are the ion's flight time and flight distance, and  $t_0$  is the offset on the time-of-flight, which is instrument-specific and occurs due to delays by cable distances and electronic devices. This offset can be obtained by comparing the measured values with the expected values from the periodic table of isotopes.

Figure 3 shows the difference between corrected (orange curve) and uncorrected (blue curve) TOF data for a pure W aFIM dataset. The peaks in the mass spectrum present a wider distribution when these are not corrected. The proposed polynomial was used to calculate the mass-to-charge ratio from the time-of-flight based on the impact position, assuming that the centre of the projection is simply the centre of the detector. The individual isotopes are readily distinguishable in the corrected mass spectrum, and the mass-to-charge values are near their expected position. Knowing the value of the W isotopes, we can correct their shift by calculating the value of  $t_0$  from Equation 2.

This approach is not meant to replace existing protocols in commercial software. However, it can be seen as an alternative when the background level is too high to deploy these existing methods.



**Fig. 2.** Flight distance as a function of the detector impact position for simulated data from Ref Loi et al. (2013) along with fitted polynomial for all the data. Insets are the ratio of the actual flight distance to the predicted from the polynomial fit for each set of data (top), for a polynomial obtained with the average of the fitting parameters obtained for all the fitted data (middle), and obtained from the Pythagoras theorem (bottom).



**Fig. 3.** Comparison of an aFIM experiment between uncorrected data (blue) and time-of-flight corrected data

(orange) of a W tip using the proposed polynomial with  $t_0 = -21.65 \text{ ns}$ .

### ***Correlation filtering***

After the TOF is corrected, further data analysis is necessary to increase the signal-to-background ratio, which is done by correlation filtering (Katnagallu et al. (2019)), based on the spatial and temporal correlations between field evaporated or field desorbed ions (De Geuser et al. (2007); Yao et al. (2010); Saxey (2011)). As indicated in Katnagallu et al. (2021), a vast majority (> 95%) of the detected ions are from the ionised imaging gas atoms. Depending on the experimental conditions, i.e., slow and controlled field evaporation aFIM experiments, we can estimate the ionisation rate of three orders of magnitude higher than the surface atoms' field evaporation rate. This ionisation forms the image and contributes to the background in the mass-to-charge spectrum. Figure 4 shows the comparison between the mass spectra of the raw data, single and multiple hits for a tungsten experiment using Ne imaging gas. Multiple hits consist of different ions arriving together on the detector in the same pulse window. The signal-to-background ratio (S/B) increases marginally for the  $W^{3+}$  peak: The raw data gives a S/B of 2.0, while the multiples have a S/B of 3.4. Here we can also see impurities of He imaging gas. In addition, there are ripple artefacts around the imaging gas peaks, which initially come from the pulsed voltage mechanism.

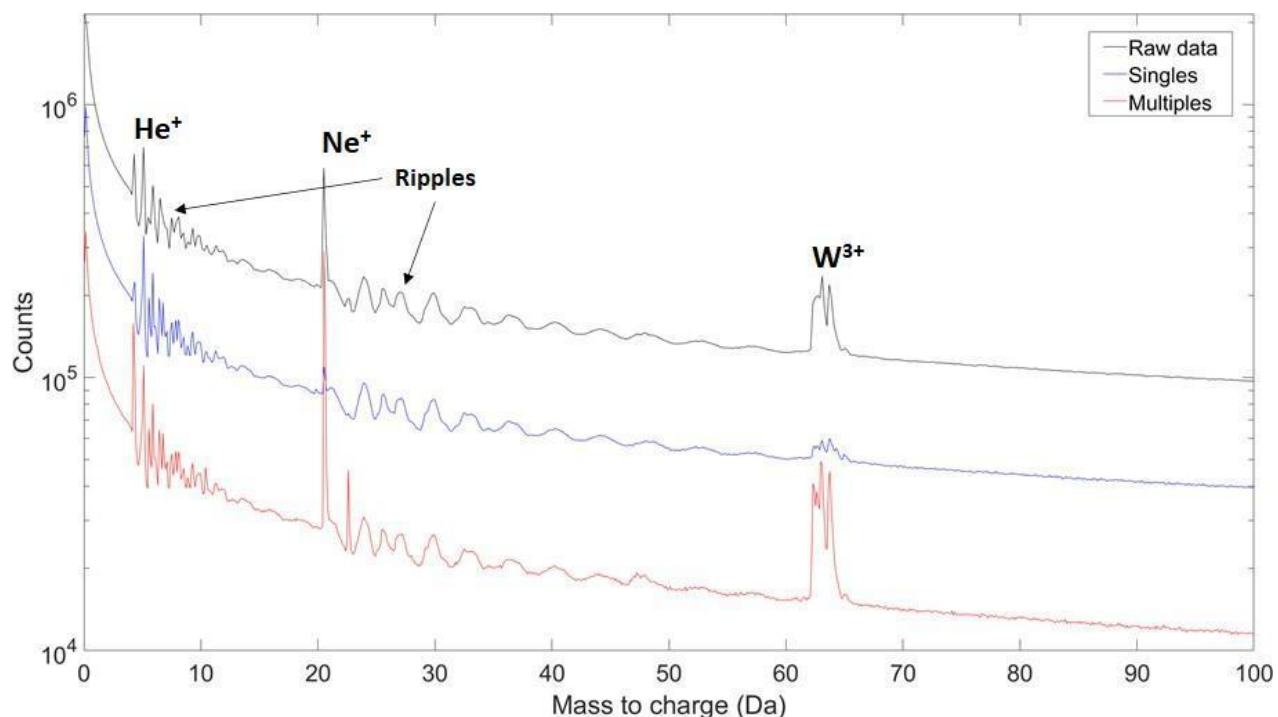


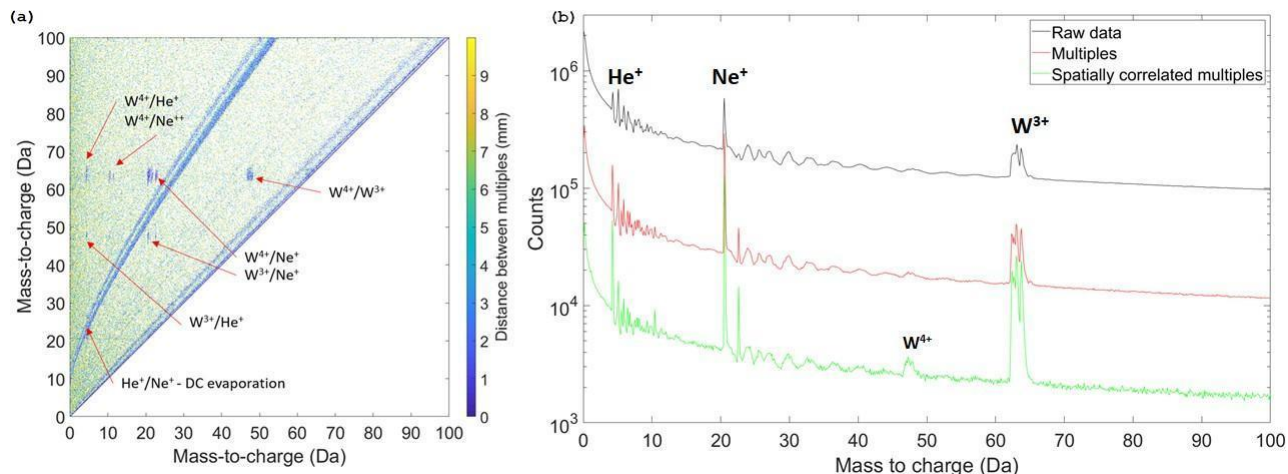
**Fig. 4.** Mass spectrum from aFIM experiment of a W tip: no post-processing analysis (black), single hits (blue), and only multiple hits (red).

We can still apply further filtering to improve the signal-to-background ratio in the multiple spectrum. Figure 5(a) shows the multiple correlation plot, sometimes referred to as the "Saxey plot" (Saxey (2011)), for the same dataset. It is the relation between the ions of a multiple event subdivided into pairs (e.g.,  $\{m_1, m_2, m_3\} \rightarrow \{(m_1, m_2), (m_1, m_3), (m_2, m_3)\}$ ). The correlation plot is color-coded according to the distance between the paired ions of the multiple events. No dissociation tracks are visible in the plot (Saxey (2011)). However, we can see a line corresponding to standing voltage or continuous evaporation of the imaging gases  $Ne^+$ ,  $He^+$ . We can also notice the co-evaporation between metal ions  $W^{4+}$ ,  $W^{3+}$ , and between metal ions and desorbing gas ions. The co-evaporations are all physically related events and show an inter-impact distance (the Euclidean distance between two ions is calculated using their detector coordinates) of less than 2 mm, depending on the magnification.

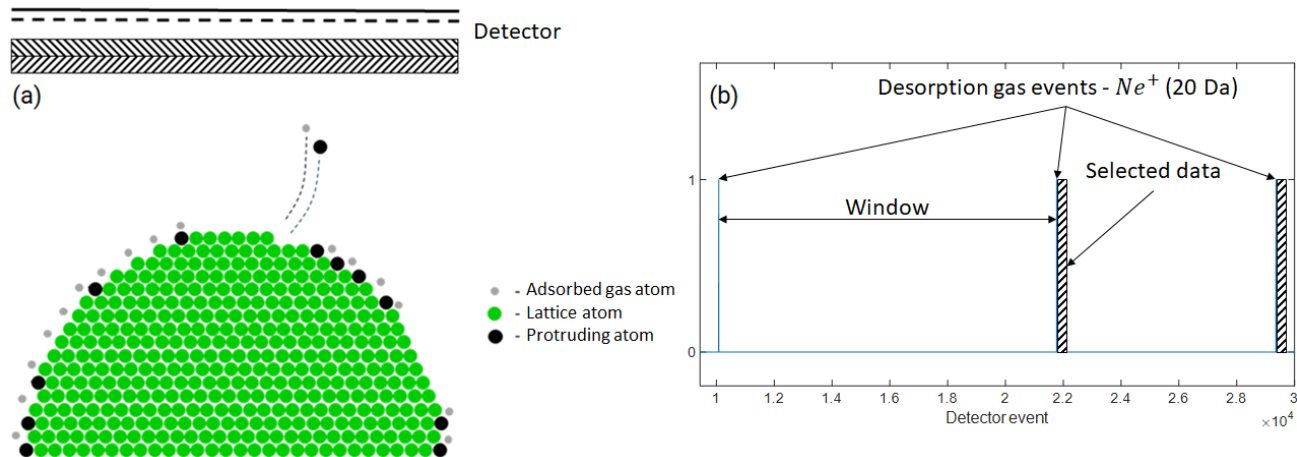
Figure 5(b) shows the comparison between the mass spectrum for all multiple events and only

those spatially correlated multiples for the pure-W dataset. The multiple events with high inter-impact distance are very likely physically independent. Consequently, the dataset is filtered by selecting the multiple events with a small inter-impact distance (e.g., lower than 2 mm (Katnagallu et al. (2019))), increasing the S/B for the  $W^{3+}$  to 11.8. It is also possible to identify the peak  $W^{4+}$  in the spectrum, previously hidden in the background. Müller et al. (1969), Kellogg et al. (1979), and Tsong et al. (1985) have shown experimental evidence of adsorption of the imaging gas into the specimen's surface due to the high electric field at cryogenic temperatures.

In addition, the gas desorption required the field evaporation of the metal ions. This desorption relation (e.g., W/Ne or W/He) can also be seen in the correlation plot of Figure 5(a). Figure 6(a) shows the schematic illustration of the correlation between the desorption of the imaging gas (measurement of the imaging gas ions, e.g.,  $Ne^+$  at 20 Da) and the field evaporation of the metal ions. We can pinpoint the most likely moments when the field evaporation of a surface atom occurred by looking for these multiple events correlated with the desorption of the imaging gas. Experimentally, we extract a specific amount of data after the imaging gas ions are measured (desorption) within the multiple events, in other words, we filter the spatially correlated multiples (green curve) by their correlation with the measurement/desorption of the imaging gas. It is a temporal filtering of the spatially correlated multiples. The data is only selected if measured close to an imaging gas desorption event, i.e., imaging gas ion detected by the time-of-flight spectrometer. The region between two desorption gas events is defined as a "window", and the amount of data selected after such desorption events is proportional to the window size (e.g., 1% of the events within the window region), as shown in Figure 6(b). The selected data region starts right after the imaging gas ion measurement (i.e., beginning of the window) because it correlates with the field evaporation of the metal ion.



**Fig. 5.** Relation between the multiple events and the inter-impact distance for the same data shown in Figure 4. (a) Correlation plot of the multiples organised in pairs. (b) Mass-to-charge spectrum comparison between raw data (black), only multiple hits (red), and spatially correlated multiples with less than 2 mm apart (green).



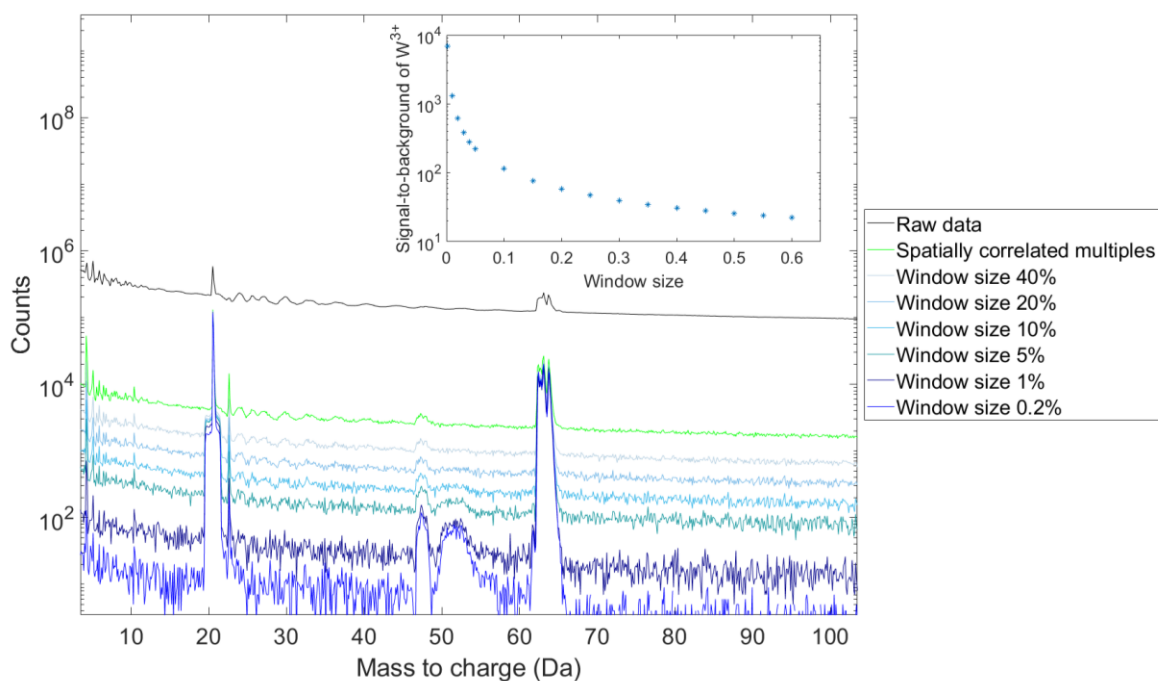
**Fig. 6.** Schematic illustration of the temporal correlation multiples filtering. (a) Correlation between desorption gas ions and field evaporation of protruding atom for the aFIM experiments. (b) Detector event index showing the window size (i.e., the region where data is extracted) between desorption gas events.

Figure 7 shows the temporal correlation of multiples for different window sizes (decreasing from top to bottom) after the desorption event for the W experiment. The analysed data is variable for each desorption event to ensure that the field evaporation event correlated with the field desorption is captured. In this case, on average, 0.2% window size means 4 multiple events, and 40% gives an average of 729 multiple events measured per window by the detector. The S/B increases substantially

for smaller window sizes, reaching values of  $7 \times 10^3$  for the  $W^{3+}$ . Window size smaller than 0.2% would not be statistically representative due to the amount of data filtered out. The following temporal correlation results were done with a 0.2% window size.

### Chemical identification

We can now compare the S/B for each filtering method for the tungsten experiment. Figure 8 compares the spectra without filtering and using only multiples, spatially correlated multiples, and spatially/temporally correlated multiples. We can see a significant decrease in the background of the mass-to-charge spectrum. In addition, the  $W^{4+}$  and the  $WNe^{4+}$  peaks start to be visible for the spatially and temporally correlated multiples methods, respectively, and the S/B increases from 2 of the raw data to  $7 \times 10^3$  when using the temporal correlation filtering for the  $W^{3+}$  peak. This post-processing data analysis makes extracting the chemical information for specific atoms of the recreated FIM images easier and more reliable.



**Fig. 7.** Comparison between different window sizes for the temporal correlation filtering for the same data shown in Figure 4. The window size decreases from 40% to 0.2% from top to bottom. Inset: shows the signal-to-background of each window size for the  $W^{3+}$ .

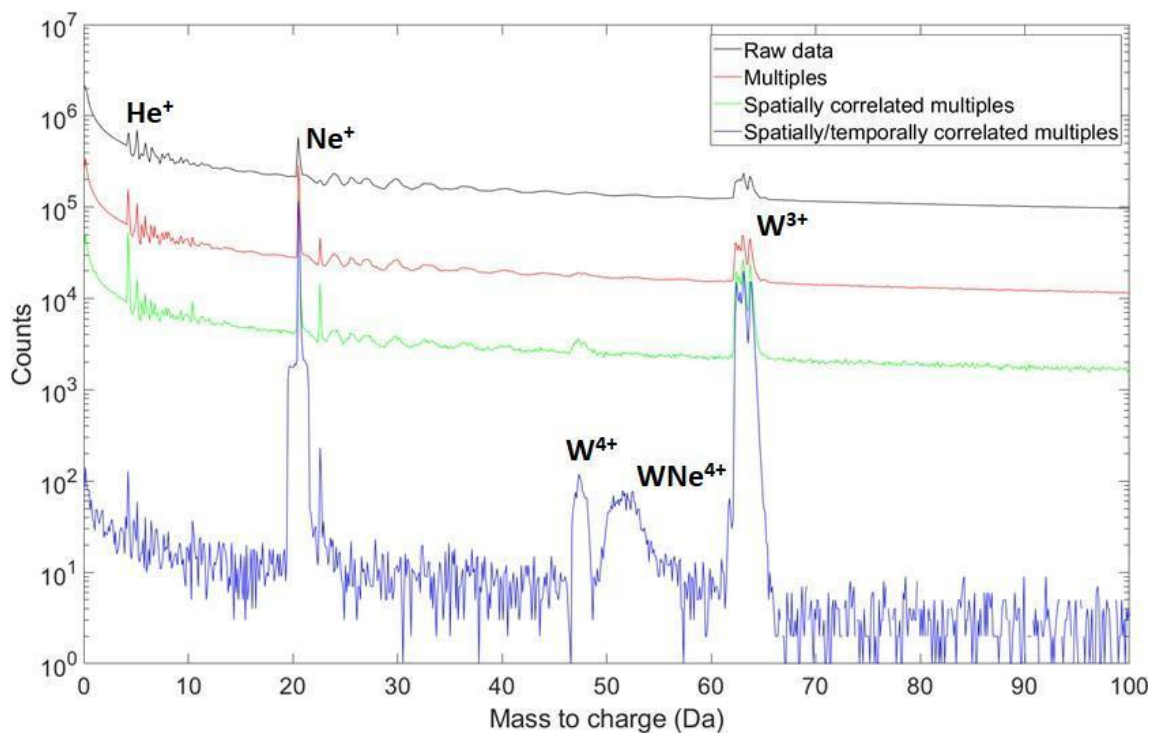


**Fig. 8.** Mass-to-charge spectrum for the different filtering methods for the same data shown in Figure 4: untreated data (black), only multiple hits (red), spatially correlated multiples (green), and spatially and temporally correlated multiples (blue).

#### *Application on amorphous alloy $Co_{68}Ta_7B_{25}$*

Finally, we use the same approach for a more complex system, the metallic glass  $Co_{68}Ta_7B_{25}$ . Each element is well separated in the mass-to-charge spectrum, for instance, 5 and 5.5 Da for  $B^{++}$ , 29.5 Da for  $Co^{++}$ , and 60.3 Da for  $Ta^{3+}$ . They also have very different ion masses, which means different mass resolutions (Rousseau et al. (2020)). Figure 9 shows the mass spectrum using different filtering methods. The S/B did not improve as much as the W case. Comparing the spatially correlated multiples with the temporal correlation, the S/B for the  $Co^{2+}$  changed from 8.21 to 38.5.

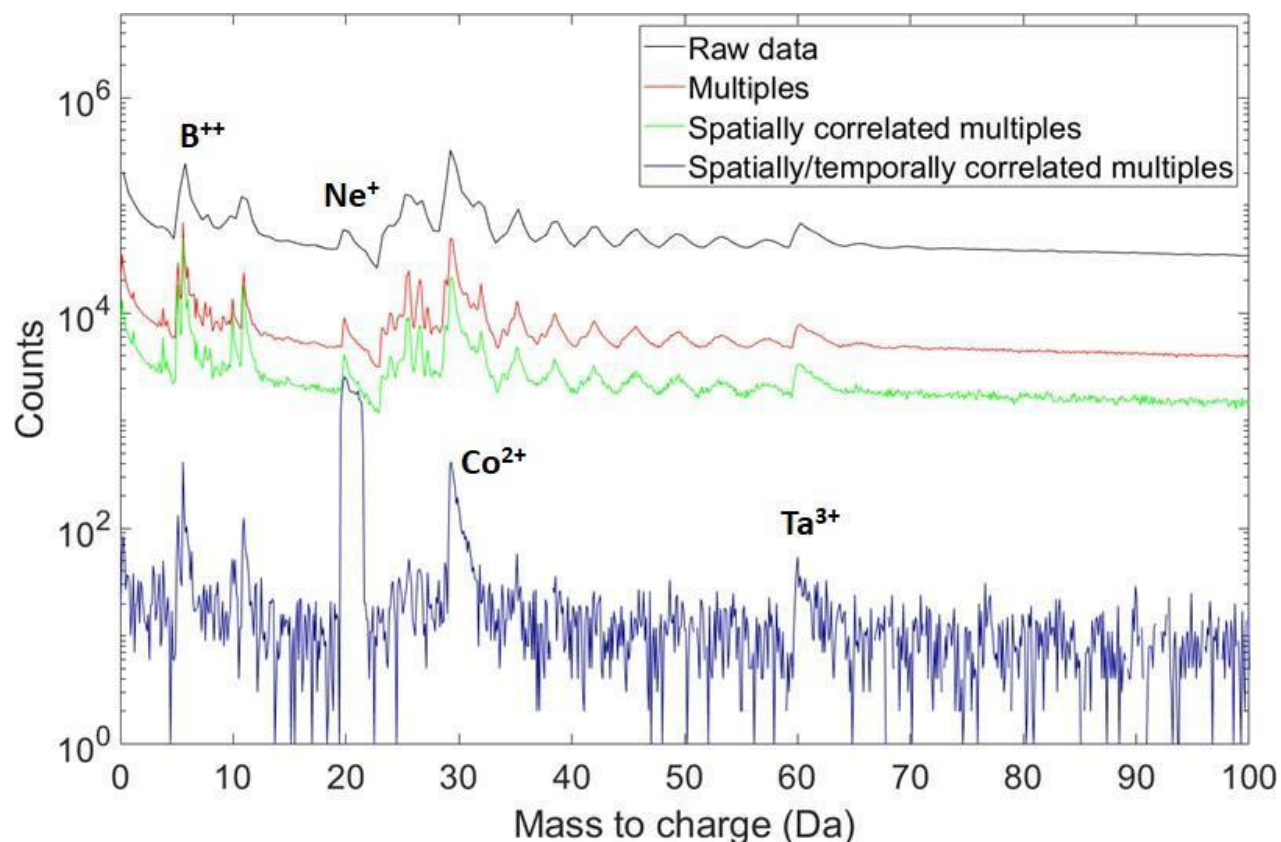


**Fig. 9.** Mass spectrum of the CoTaB alloy using the different filtering methods: untreated data (black), only multiple hits (red), spatially correlated multiples (green), and spatially and temporally correlated multiples (blue).

## Summary and discussion

Herein, we proposed methods to handle some current challenges in processing aFIM data.

### *TOF correction*

Nowadays, most APT experiments have their TOF corrected via the iterative procedure of the commercial software AP Suite. We proposed an alternative correction based on electrostatic simulations for different geometries and launch angles to estimate the flight length via a simple polynomial. In principle, this correction applies to any APT data, but we show the polynomial applied for aFIM experiments acquired by using the APT mode of the LEAP 5000XS. Figure 3 shows the result of the correction for an aFIM experiment of pure-W, in which the S/B was significantly low. The uncorrected data (blue curve) has very broad peaks shifted more than 5 Da from the expected value. The polynomial algorithm makes the isotopes distinguishable and corrects

their shift.

Further refinement of the TOF via a more involved bowl correction may be necessary, including via the conventional approach outlined in Larson et al. (2013). The method we introduce here may also be too simplistic in some cases. However, its computational cost is minimal, and it can already provide sufficient improvement in the signal-to-background ratio to enable further corrections.

### *Mass-to-charge spectrum filtering*

Although the imaging gas field ionisation contributes to the image quality, the higher pressure and ionisation rate will also contribute significantly to the high background found in the mass-to-charge spectrum of aFIM experiments. Therefore, post-processing of the data is essential to remove most of the background and extract the chemical information of the imaged atoms. Figure 4 shows how the usage of the multiple events can already improve the signal-to-background from 2.0 to 3.4 for the  $W^{3+}$ . Due to the constant ionisation events, the field evaporation is expected to be correlated to the multiple events. In addition, we can note that even just adding 99.999% pure neon as the imaging gas, we still measure residual He imaging gas from previous experiments or leak in the mixing chamber setup. A mixing gas composition can help image more complex alloys due to different best image fields (Panitz (1982); Akre et al. (2009)). However, the experiment temperature will be limited by the higher condensation temperature of each gas involved.

The visible ripples across all spectra following the imaging gas peaks can be associated with dynamic effects from the HV pulse discussed in detail by Rousseau et al. (2020) or imperfect filtering of the HV pulse leaving trailing low-amplitude pulses after the main pulse. These ripples can make it more challenging to identify chemical elements with a mass-to-charge close to the main imaging gas. These ripples do not appear with aFIM performed in laser mode, as discussed previously (Katnagallu et al. (2021)).

When looking through all the combinations of multiple hits, we can still filter out those not

corresponding to the field evaporation of the metal ion. Spatial correlation filtering removes the physically unrelated events by calculating the distance between the ions when hitting the detector, e.g., two ionised imaging gas in the same pulsed window. Temporal correlation filtering uses the desorption of the imaging gas to pinpoint the moments that field evaporation occurred. This correlation can also be seen experimentally via the multiple correlation plot (e.g., W/Ne or W/He) in Figure 6(b). Figure 8 shows the improvement in the S/B when these algorithms are implemented for the W sample. It goes from 2.0 to  $7 \times 10^3$  for the  $W^{3+}$  and from indistinguishable to 6.1 for the peak  $W^{4+}$ . For smaller window sizes, the S/B increases for all peaks, and molecular ions ( $WNe^{4+}$ ) are visible (Müller et al. (1969)). However, when the same algorithm is applied to a more complex alloy like  $Co_{68}Ta_7B_{25}$ , the S/B does not increase in the same proportion as in the tungsten experiments, going from 8.21 to 38.5 for the  $Co^{2+}$  peak. This could be due to a more complex evaporation process, associated with the variety of neighborhoods of the surface atoms at the time of field evaporation, as well as an average lower evaporation field for Co, Ta, and B, in particular in comparison to the field necessary to desorb the imaging gas from the surface.

The exact value of the detection efficiency using this filtering method is not trivial to extract. As mentioned previously, aFIM is performed in the LEAP 5000 XS instrument, which has a detection efficiency of around 80%. However, most of the ions detected in an aFIM experiment arise from the field ionisation of the imaging gas atoms, which provides the image of the surface atoms. Therefore, aFIM could have a higher imaging efficiency than APT, since losing the field ionisation events would only imply a small change in the contrast of the imaged surface atoms, the atom on the surface could still be imaged. The key limitation is the detection of the ion from the field evaporated surface atoms, because, despite the filtering method having significantly improved the S/B, the detection efficiency decreased as noticeable by the reduction of the number of ions detected for each peak in Figure 8 and Figure 9, along with the association of an imaged position with a time-of-flight. For the case of

W, the difference between the raw spectrum and the spatially/temporal correlated multiples is about an order of magnitude. Meanwhile, for the  $Co_{68}Ta_7B_{25}$  experiment, there was a decrease of 2 orders of magnitude. One way to increase the detection efficiency and reliability is by using additional information for the identification, for instance, density functional theory (DFT) calculations can give insights into the brightness of the imaged surface atoms, or the measurement of the atomic radius of the imaged atoms.

The relatively low detection efficiency can impact material science applications since it can fail to detect the desired/specific ions, such as solute segregation to vacancies of Morgado et al. work (Morgado et al. (2021)). In this case, aFIM experiments assisted with DFT calculations were used to identify the Ta solute ions, seen as brighter surface atoms in the FIM images. Further developments in the filtering/identification are necessary to improve the detection efficiency to expand aFIM applicability.

## **Conclusion**

Analytical FIM has the potential for unraveling long-standing problems in materials science. However, there remain many challenges in the processing of complex data. The background could be significantly reduced with spatial and temporal correlation filtering, with S/B improvements up to three orders of magnitude. Further refinements are needed to facilitate the routine application of aFIM beyond qualitative information, as is often done at the moment in combination with three-dimensional FIM, for instance (Klaes et al. (2021)). Information regarding the brightness of each imaged atom is currently not exploited, and monitoring the brightness change for each imaged atom could help associate an image position to a detected ion moment. Nevertheless, aFIM is a promising technique that could improve our understanding of trajectory aberration found in APT.

**Acknowledgements** The authors are thankful to Drs Shyam Katnagallu & Isabelle Mouton for fruitful discussions and kick-starting some of this work. This work was supported by a scholarship from The International Max Planck Research School for Interface Controlled Materials for Energy Conversion (IMPRS-

SurMat) for F.F.M. We appreciate the technical support of U. Tezins, C. Bross and A. Sturm at the APT/FIB facilities at Max-Planck-Institut für Eisenforschung. LTS & BG author acknowledges financial support from the ERC CoG-SHINE-771,602. The authors acknowledge support by the German National Science Foundation (DFG) within the SPP-1594 (DE796/9-2, RA 659/28-2 and SCHN 735/35-2).

Competing interests: the author(s) declare none.

## References

- Akre, J., Danoix, F., Leitner, H. & Auger, P.** (2009). The morphology of secondary-hardening carbides in a martensitic steel at the peak hardness by 3DFIM, *Ultramicroscopy* **109**, 518–523.
- Allen, L.J., D’Alfonso, A.J., Freitag, B. & Klenov, D.O.** (2012). Chemical mapping at atomic resolution using energy-dispersive x-ray spectroscopy, *MRS Bulletin* **37**, 47–52.
- Block, J., Drachsel, W. & Gorodetskii, V.** (1994). Direct imaging of catalytic surface reactions in the field-ion microscope: The oxidation of hydrogen on platinum. *Recl. Trav. Chim. Pays-Bas*, **113**, 444-447, URL <https://doi.org/10.1002/recl.19941131007>.
- Cerezo, A., Clifton, P., Gombert, A. & Smith, G.** (2007). Aspects of the performance of a femtosecond laser-pulsed 3-dimensional atom probe, *Ultramicroscopy* **107**, 720–725, URL <https://doi.org/10.1016/j.ultramic.2007.02.025>.
- De Geuser, F., Gault, B., Bostel, A. & Vurpillot, F.** (2007). Correlated field evaporation as seen by atom probe tomography, *Surface Science* **601**, 536–543, URL <http://www.scopus.com/inward/record.url?eid=2-s2.0-33846061166&partnerID=tZOtx3y1>
- Deconihout, B., Vurpillot, F., Gault, B., Da Costa, G., Bouet, M., Bostel, A., Blavette, D., Hideur, A., Martel, G. & Brunel, M.** (2007). Toward a laser assisted wide-angle tomographic atom-probe, *Surface and Interface Analysis* **39**, 278–282, URL <https://analyticalsciencejournals.onlinelibrary.wiley.com/doi/10.1002/sia.2491>.
- Evertz, S., Schnabel, V., Köhler, M., Kirchlechner, I., Kontis, P., Chen, Y.T., Soler, R., Jaya, B.N., Kirchlechner, C., Music, D., Gault, B., Schneider, J.M., Raabe, D. & Dehm, G.** (2020). Review on Quantum Mechanically Guided Design of Ultra-Strong Metallic Glasses, *Frontiers in Materials* **7**.
- Gault, B., Chieramonti, A., Cojocaru-Mirédin, O., Stender, P., Dubosq, R., Freysoldt, C., Makineni, S.K., Li, T., Moody, M. & Cairney, J.M.** (2021a). Atom probe tomography, *Nature Reviews Methods Primers* **1**, URL <https://doi.org/10.1038/s43586-021-00047-w>.
- Gault, B., Klaes, B., Morgado, F.F., Freysoldt, C., Li, Y., De Geuser, F., Stephenson, L.T. & Vurpillot, F.** (2021b). Reflections on the spatial performance of atom probe tomography in the analysis of atomic

neighborhoods, *Microscopy and Microanalysis* 1–11.

**Gault, B., Moody, M.P., Cairney, J.M. & Ringer, S.P.** (2012a). New York, NY: Springer New York.

**Goris, B., De Backer, A., Van Aert, S., Gómez-Graña, S., Liz-Marzán, L.M., Van Tendeloo, G. & Bals, S.** (2013). Three-dimensional elemental mapping at the atomic scale in bimetallic nanocrystals, *Nano Letters* **13**, 4236–4241, URL <https://pubs.acs.org/doi/abs/10.1021/nl401945b>.

**Itakura, M., Watanabe, N., Nishida, M., Daio, T. & Matsumura, S.** (2013). Atomic-resolution x-ray energy-dispersive spectroscopy chemical mapping of substitutional dy atoms in a high-coercivity neodymium magnet, *Japanese Journal of Applied Physics* **52**, copyright: Copyright 2013 Elsevier B.V., All rights reserved.

**Jentsch, T., Drachsel, W. & Block, J.H.** (1981). Copper cluster ions in photon-induced field ionization mass spectra, *International Journal of Mass Spectrometry and Ion Physics* **38**, 215-222, URL [https://doi.org/10.1016/0020-7381\(81\)80068-X](https://doi.org/10.1016/0020-7381(81)80068-X).

**Katnagallu, S., Morgado, F.F., Mouton, I., Gault, B. & Stephenson, L.T.** (2021). Three-dimensional atomically resolved analytical imaging with a field ion microscope, *Microscopy and Microanalysis* 1–16.

**Katnagallu, S., Stephenson, L.T., Mouton, I., Freysoldt, C., Subramanyam, A.P.A., Jenke, J., Ladines, A.N., Neumeier, S., Hammerschmidt, T., Drautz, R., Neugebauer, J., Vurpillot, F., Raabe, D. & Gault, B.** (2019). Imaging individual solute atoms at crystalline imperfections in metals, *New Journal of Physics* **21**, 123020, URL <https://doi.org/10.1088/1367-2630/ab5cc4>.

**Kellogg, G.L. & Tsong, T.T.** (1979). Pulsed-laser atom-probe field-ion microscopy, *Journal of Applied Physics* **51**, 1184, URL <http://www.scopus.com/inward/record.url?eid=2-s2.0-0018979293&partnerID=tZOtx3y1>.

**Kelly, T.F., Gribb, T.T., Olson, J.D., Martens, R.L., Shepard, J.D., Wiener, S.A., Kunicki, T.C., Ulfing, R.M., Lenz, D.R., Strennen, E.M., Oltman, E., Bunton, J.H. & Strait, D.R.** (2004). First data from a commercial local electrode atom probe (LEAP), *Microscopy and microanalysis: the official journal of Microscopy Society of America, Microbeam Analysis Society, Microscopical Society of Canada* **10**, 373–383, URL <http://www.scopus.com/inward/record.url?eid=2-s2.0-3042585904&partnerID=tZOtx3y1>.

**Kelly, T.F. & Larson, D.J.** (2012). Atom probe tomography 2012, *Annual Review of Materials Research* **42**, 1–31, URL <https://doi.org/10.1146/annurev-matsci-070511-155007>.

**Kim, Y.M., Lee, K., Fu, L., Oh, M.W., Yang, S.H., Ning, S., Han, G., Kim, M., Kim, J.S., Jeong, M., Jang, J., Lee, E., Okunishi, E., Sawada, H., Kim, S., Pennycook, S., Lee, Y. & Kim, S.** (2021). Atomic-scale chemical mapping of copper dopants in  $\text{Bi}_2\text{Te}_{2.7}\text{Se}_{0.3}$  thermoelectric alloy, *Materials Today Physics* **17**, 100347, URL <https://www.sciencedirect.com/science/article/pii/S2542529321000080>.

- Kingham, D.R.** (1982). The post-ionization of field evaporated ions: A theoretical explanation of multiple charge states, *Surface Science* **116**, 273–301.
- Klaes, B., Renaux, J., Lardé, R., Delaroche, F., Morgado, F.F., Stephenson, L.T., Gault, B. & Vurpillot, F.** (2021). Analytical three-dimensional field ion microscopy of an amorphous glass febsi, *Microscopy and Microanalysis* 1–9.
- Kontis, P., Köhler, M., Evertz, S., Chen, Y.T.T., Schnabel, V., Soler, R., Bednarick, J., Kirchlechner, C., Dehm, G., Raabe, D., Schneider, J.M. & Gault, B.** (2018). Nano-laminated thin film metallic glass design for outstanding mechanical properties, *Scripta Materialia* **155**, 73–77.
- Krishnaswamy, S.V., McLane, S.B. & Müller, E.W.** (1975). Aiming performance of the atom probe, *Review of Scientific Instruments* **46**, 1237–1240.
- Larson, D.J., Prosa, T.J., Ulfing, R.M., Geiser, B.P. & Kelly, T.F.** (2013). Data processing and reconstruction, *Local Electrode Atom Probe Tomography*, 109–162, Springer New York, URL [https://doi.org/10.1007/978-1-4614-8721-0\\_5](https://doi.org/10.1007/978-1-4614-8721-0_5).
- Larson, D.J., Gault, B., Geiser, B.P., De Geuser, F. & Vurpillot, F.** (2013a) Atom probe tomography spatial reconstruction: Status and directions, *Current Opinion in Solid State and Materials Science* **17**, 236–247, URL <https://doi.org/10.1016/j.cossms.2013.09.002>.
- Loi, S.T., Gault, B., Ringer, S.P., Larson, D.J. & Geiser, B.P.** (2013). Electrostatic simulations of a local electrode atom probe: the dependence of tomographic reconstruction parameters on specimen and microscope geometry., *Ultramicroscopy* **132**, 107–113, URL <http://www.scopus.com/inward/record.url?eid=2-s2.0-84884206901&partnerID=tZOtx3y1>.
- Miller, M.K.** (1987). The effects of local magnification and trajectory aberrations on atom probe analysis. *Journal de Physique Colloques*, URL <http://dx.doi.org/10.1051/jphyscol:1987692>.
- Miller, M.K.** (2005). Atom probe tomography, *Handbook of Microscopy for Nanotechnology*, 227– 246, Kluwer Academic Publishers, URL [https://doi.org/10.1007/1-4020-8006-9\\_8](https://doi.org/10.1007/1-4020-8006-9_8).
- Miller, M.K. & Forbes, R.G.** (2014). *The Art of Specimen Preparation*, 189–228, Boston, MA: Springer US, URL [https://doi.org/10.1007/978-1-4899-7430-3\\_4](https://doi.org/10.1007/978-1-4899-7430-3_4).
- Morgado, F.F., Katnagallu, S., Freysoldt, C., Klaes, B., Vurpillot, F., Neugebauer, J., Raabe, D., Neumeier, S., Gault, B. & Stephenson, L.T.** (2021). Revealing atomic- scale vacancy-solute interaction in nickel, *Scripta Materialia* **203**, 114036, URL <https://www.sciencedirect.com/science/article/pii/S135964622100316X>.
- Müller, E.W.** (1951). Das feldionenmikroskop, *Zeitschrift für Physik* **131**, 136–142, URL <https://doi.org/10.1007/bf01329651>.

- Müller, E.W.** (1956). Resolution of the atomic structure of a metal surface by the field ion microscope, *Journal of Applied Physics* **27**, 474–476.
- Müller, E. W. & Young, R. D.** (1961). Determination of Field Strength for Field Evaporation and Ionization in the Field Ion Microscope, *Journal of Applied Physics* **32**, 2425-2428  
URL <https://doi.org/10.1063/1.1777085>.
- Müller, E. W. & Tsong, T. T.** (1969). *Field-Ion Microscopy: Principles and Applications* (New York: Elsevier).
- Müller, E.W., McLane, S. & Panitz, J.** (1969). Field adsorption and desorption of helium and neon, *Surface Science* **17**, 430–438, URL <https://www.sciencedirect.com/science/article/pii/0039602869901101>.
- Müller, E.W., Panitz, J.A. & McLane, S.B.** (1968). The atom probe field ion microscope, *Review of Scientific Instruments* **39**, 83–86, URL <https://doi.org/10.1063/1.1683116>.
- Panitz, J.A.** (1982). Field-ion microscopy-a review of basic principles and selected applications, *Journal of Physics E: Scientific Instruments* **15**, 1281–1294, URL <https://doi.org/10.1088/0022-3735/15/12/004>.
- Pareige, C., Lefebvre-Ulrikson, W., Vurpillot, F. & Sauvage, X.** (2016). Atom probe tomography: Put theory into practice, W. Lefebvre-Ulrikson, F. Vurpillot & X. Sauvage (eds.), *Atom Probe Tomography*, 123–154, Academic Press, URL <https://www.sciencedirect.com/science/article/pii/B978012804647000005X>.
- Robertson, A.W. & Warner, J.H.** (2013). Atomic resolution imaging of graphene by transmission electron microscopy, *Nanoscale* **5**, 4079, URL <https://doi.org/10.1039/c3nr00934c>.
- Rousseau, L., Normand, A., Morgado, F.F., Stephenson, L., Gault, B., Tehrani, K. & Vurpillot, F.** (2020). Dynamic Effects in Voltage Pulsed Atom Probe, *Microscopy and Microanalysis* **26**, 1133–1146, URL <https://www.cambridge.org/core/journals/microscopy-and-microanalysis/article/abs/dynamic-effects-in-voltage-pulsed-atom-probe/90AB9545A731B856E554548055946C0F>.
- Saxey, D.** (2011). Correlated ion analysis and the interpretation of atom probe mass spectra, *Ultramicroscopy* **111**, 473–479, URL <https://www.sciencedirect.com/science/article/pii/S0304399110003116>, special Issue: 52nd International Field Emission Symposium.
- Schmidt, W.A., Suchorski, Y. & Block, J.H.** (1994). New aspects of field adsorption and accommodation in field ion imaging, *Surface Science*, **301**, 52-60, URL [https://doi.org/10.1016/0039-6028\(94\)91287-4](https://doi.org/10.1016/0039-6028(94)91287-4).
- Schnabel, V., Köhler, M., Evertz, S., Gamcova, J., Bednarcik, J., Music, D., Raabe, D. & Schneider, J.M.** (2016). Revealing the relationships between chemistry, topology and stiffness of ultrastrong Co-based metallic glass thin films: A combinatorial approach, *Acta Materialia* **107**, 213–219.

- Sebastian, J.T., Hellman, O.C. & Seidman, D.N.** (2001). New method for the calibration of three-dimensional atom-probe mass spectra, *Review of Scientific Instruments* **72**, 2984–2988.
- Seidman, D.N.** (2007). Three-dimensional atom-probe tomography: Advances and applications, *Annual Review of Materials Research* **37**, 127–158, URL <https://doi.org/10.1146/annurev.matsci.37.052506.084200>.
- Sweeney, J.H. & Tsong, T.** (1981). Measurement of enhancement in field ionization of helium and neon by self-field adsorption, *Surface Science Letters* **104**, L179–L184, URL <https://www.sciencedirect.com/science/article/pii/0167258481901730>.
- Tsong, T. T., & Liou, Y.** (1985). Time-of-Flight Energy and Mass Analysis of Metal-Helide Ions and Their Formation and Dissociation. *Physical Review Letters* **55**, 2180–2183. URL <https://doi.org/10.1103/physrevlett.55.2180>.
- Tsong, T.T.** (1990). Atom-Probe Field Ion Microscopy: Field Ion Emission, and Surfaces and Interfaces at Atomic Resolution, Cambridge University Press.
- Vurpillot, F., Danoix, F., Gilbert, M., Koelling, S., Dagan, M. & Seidman, D.N.** (2017). True atomic-scale imaging in three dimensions: A review of the rebirth of field-ion microscopy, *Microscopy and Microanalysis* **23**, 210–220.
- Wei, J., Feng, B., Ishikawa, R., Yokoi, T., Matsunaga, K., Shibata, N. & Ikuhara, Y.** (2021). Direct imaging of atomistic grain boundary migration, *Nature Materials* **20**, 951–955, URL <https://doi.org/10.1038/s41563-020-00879-z>.
- Yao, L., Gault, B., Cairney, J.M.M. & Ringer, S.P.P.** (2010). On the multiplicity of field evaporation events in atom probe: A new dimension to the analysis of mass spectra, *Philosophical Magazine Letters* **90**, 121–129, URL <http://www.scopus.com/inward/record.url?eid=2-s2.0-76449120386&partnerID=tZOtx3y1> <http://www.scopus.com/inward/record.url?eid=2-s2.0-76449120386&partnerID=40&md5=da48ab1f8365fcb70fb7bdfbf66ec917>.
- Zhang, Q., He, X., Shi, J., Lu, N., Li, H., Yu, Q., Zhang, Z., Chen, L.Q., Morris, B., Xu, Q., Yu, P., Gu, L., Jin, K. & Nan, C.W.** (2017). Atomic-resolution imaging of electrically induced oxygen vacancy migration and phase transformation in SrCoO<sub>2.5</sub>- $\sigma$ , *Nature Communications* **8**, URL <https://doi.org/10.1038/s41467-017-00121-6>.
- Zhou, J., Yang, Y.Y., Yang, Y.Y., Kim, D.S., Yuan, A., Tian, X., Ophus, C., Sun, F., Schmid, A.K., Nathanson, M., Heinz, H., An, Q., Zeng, H., Ercius, P. & Miao, J.** (2019). Observing crystal nucleation in four dimensions using atomic electron tomography, *Nature* **570**, 500–503.